

# Bridging Discrete Planning and Continuous Execution for Redundant Robot Manipulators

Teng Yan\*, Yue Yu\*, Yihan Liu\*, Bingzhuo Zhong\*,\*\*

\* *The Thrust of Artificial Intelligence, Information Hub, Hong Kong University of Science and Technology (Guangzhou), Guangzhou 511400, China (e-mail: tyan497@connect.hkust-gz.edu.cn, yyu704@connect.hkust-gz.edu.cn, yliu135@connect.hkust-gz.edu.cn).*

\*\* *The Thrust of Intelligent Transportation, System Hub, Hong Kong University of Science and Technology (Guangzhou), Guangzhou 511400, China (e-mail: bingzhuoz@hkust-gz.edu.cn)*

---

**Abstract:** Voxel-grid reinforcement learning is widely adopted for path planning in redundant manipulators due to its simplicity and reproducibility. However, direct execution through point-wise numerical inverse kinematics on 7-DoF arms often yields step-size jitter, abrupt joint transitions, and instability near singular configurations. This work proposes a bridging framework between discrete planning and continuous execution without modifying the discrete planner itself. On the planning side, step-normalized 26-neighbor Cartesian actions and a geometric tie-breaking mechanism are introduced to suppress unnecessary turns and eliminate step-size oscillations. On the execution side, a task-priority damped least-squares (TP-DLS) inverse kinematics layer is implemented. This layer treats end-effector position as a primary task, while posture and joint centering are handled as subordinate tasks projected into the null space, combined with trust-region clipping and joint velocity constraints. On a 7-DoF manipulator in random sparse, medium, and dense environments, this bridge raises planning success in dense scenes from about 0.58 to 1.00, shortens representative path length from roughly 1.53 m to 1.10 m, and—while keeping end-effector error below 1 mm—reduces peak joint accelerations by over an order of magnitude, substantially improving the continuous execution quality of voxel-based RL paths on redundant manipulators.

*Keywords:* Robot manipulators, Redundant robots, Motion planning, Path planning, Reinforcement learning, Trajectory generation, Autonomous systems, Collision avoidance

---

## 1. INTRODUCTION

Redundant robot manipulators are widely used in flexible and semi-structured environments, where they must generate collision-free motions while respecting joint limits, avoiding singularities, and staying within actuator bounds. Classical sampling- and optimisation-based planners offer strong guarantees but rely on accurate models and careful tuning, which makes frequent layout or task changes expensive. Reinforcement-learning (RL) planners on voxelised workspaces therefore become attractive: they learn a reusable value function on a finite state-action space and answer motion queries by table look-up. A common formulation discretises the task space into a voxel grid, defines a finite neighbourhood action set, and trains an RL agent to move the end-effector from a start voxel to a goal voxel while avoiding occupied cells. The output is a discrete Cartesian path. When such a path is executed on a seven-degree-of-freedom (7-DoF) redundant arm by point-wise numerical inverse kinematics (IK), however, planning and execution are misaligned: each waypoint is solved

independently, step sizes fluctuate, joint configurations can jump, and the solution is highly sensitive to singularities and joint limits. Trajectories may converge numerically but remain dynamically implausible.

Figure 1 summarises the gap considered in this work. Classical motion planning answers *Question 1: How to reach the goal?* by producing a feasible collision-free path. For redundant manipulators in cluttered environments, it is equally important to answer *Question 2: How to reach the goal better?*, i.e., along a path that is short, smooth, and compliant with safety and actuation constraints. This paper focuses on this second question at the interface between a voxel-based RL planner and the continuous execution layer of a 7-DoF arm.

A further difficulty stems from the geometry of the discrete action set. In a three-dimensional voxel grid, the standard 26-neighbourhood mixes axis-aligned, face-diagonal, and space-diagonal moves with different Euclidean lengths. Combined with  $\epsilon$ -greedy exploration and approximate value functions, this anisotropy produces “saw-tooth” paths where long and short steps are interleaved and the end-effector oscillates around obstacles or meanders in

---

\* This work was supported in part by Youth S&T Talent Support Programme of GDSTA (SKXRC2025468).

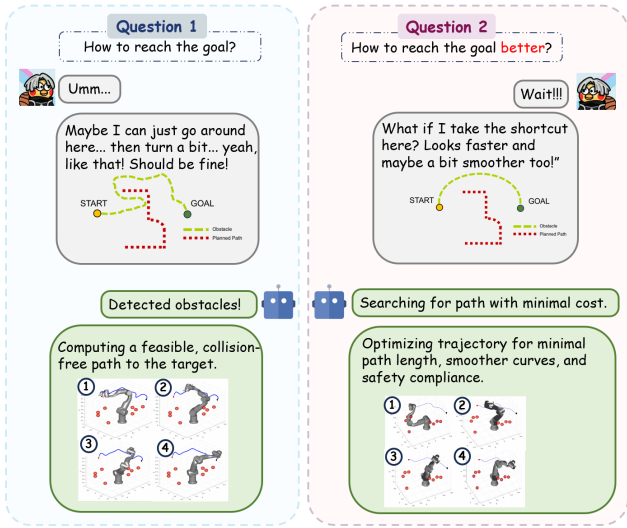


Fig. 1. **Conceptual motivation.** Left: classical planning - feasible collision-free path (**Q1**); Right: practical deployment - high-quality path (**Q2**). The proposed method meets the second requirement by bridging a voxel RL planner with a continuous execution layer on a redundant manipulator.

unproductive directions. Paths become unnecessarily long, contain redundant turns, and visit homotopy classes that are hard to track smoothly in joint space.

Existing techniques address only parts of this interface. Path smoothing and time-parameterisation fit continuous trajectories through discrete waypoints and enforce velocity and acceleration bounds, but do not correct topological artefacts such as detours or oscillations. Damped least-squares (DLS) and task-priority IK improve robustness near singularities and support secondary goals such as joint-limit avoidance, yet are usually applied as pointwise solvers and assume already smooth references. As a result, the interface between discrete planning and continuous execution is often treated as a trivial concatenation rather than a design problem.

This paper treats that interface explicitly and proposes a lightweight bridge between voxel-based RL planners and continuous execution on redundant manipulators. The RL planner is used as a black box; only the geometry of its action space and the execution layer are modified. On the planning side, the 26-neighbourhood is replaced by a step-normalized Cartesian action set with a geometric tie-breaking rule that prefers small turning angles and larger estimated clearance, regularising path geometry without changing the RL update rule. On the execution side, a TP-DLS layer tracks a globally smoothed and locally subdivided end-effector path, using joint-centering in the null space, along with norm and per-joint increment limits, to enforce trust-region-like bounds on joint updates.

The proposed bridge is evaluated on a 7-DoF manipulator in MATLAB across random environments with sparse, medium, and dense obstacle distributions. Metrics at both planning and execution levels quantify path length, turning behaviour, clearance, joint-space smoothness, and dynamic feasibility. Results show that modest modifications at the planning and execution interfaces substantially im-

prove planning success, shorten paths, and turn numerically feasible but physically unrealistic IK sequences into dynamically reasonable motions. The main contributions of this paper are:

**Mismatch analysis.** Identifies the structural mismatch between voxel-based RL paths and continuous execution on redundant manipulators, clarifying the roles of anisotropic action metrics and pointwise IK in generating artefacts.

**Bridge architecture.** Proposes a lightweight bridge that combines step-normalized 26-neighbour actions with geometric tie-breaking on the planning side and a TP-DLS execution layer with joint-centering and bounded joint updates.

**Benchmark and evidence.** Develops a benchmark suite and metric set for a 7-DoF arm and demonstrates improved path length, joint-space smoothness, and physical executability in cluttered environments.

## 2. RELATED WORK

### 2.1 RL-Based Motion Planning and Voxel Policies

Recent surveys provide comprehensive overviews of deep reinforcement learning (DRL) in robotic-manipulator motion planning and identify persistent limitations in safety, sample efficiency, and execution robustness on high-DOF systems (Elguea-Aguinaco et al., 2024; Han et al., 2023). For redundant manipulators, DRL-based frameworks have been shown to directly generate task-space motions while considering kinematic limits (Li et al., 2021). Research leveraging voxel or grid representations further demonstrates the suitability of discretized workspaces and finite action sets for RL-based planning (Landgraf et al., 2021; James et al., 2022).

A representative example in this direction is the use of RL for autonomous obstacle-avoidance path planning on six-axis robotic arms, where voxelized environments enable stable policy learning and reliable deployment (Jia et al., 2020).

Although these works validate the effectiveness of voxel and discrete-action policies, they typically focus on producing discrete end-effector paths and do not examine how such paths should be executed on redundant manipulators governed by continuous-time dynamics.

### 2.2 Redundancy Resolution and Task-Priority Control

For execution on redundant arms, damped least-squares (DLS) inverse kinematics has long been employed to bound joint velocities and mitigate singularity-induced instabilities (Deo and Walker, 1995). Task-priority control organizes multiple objectives—such as end-effector tracking, posture optimization, and safety margins—into a hierarchical structure, projecting secondary tasks into the Jacobian null space (Nakamura et al., 1987; Basso and Pettersen, 2020). These classical formulations form the mathematical basis of the task-priority DLS (TP-DLS) execution layer used in this work.

In parallel, safety-focused architectures have been proposed to encapsulate learning-based controllers within ver-

ifiable supervisory layers (Zhong et al., 2021, 2023). The present work does not introduce a new safety filter; instead, it shows that a suitably regularized TP-DLS layer, together with mild action-space constraints, already yields improved smoothness and safety when executing voxel RL policies on 7-DOF arms.

### 2.3 Trajectory Smoothing and Optimization

Beyond kinematic execution, substantial research has focused on smoothing piecewise-linear paths generated by sampling-based planners. Collision-aware spline constructions and time-parameterization approaches have been shown to reduce curvature, acceleration peaks, and discontinuities in task-space trajectories (Pan et al., 2012; Kim et al., 2020). Optimization-based methods further integrate collision avoidance and dynamic feasibility into unified formulations (Liu et al., 2021). These techniques, however, typically require solving a dedicated optimization problem for each path.

In contrast, the present work introduces a lightweight bridging mechanism. Rather than invoking a full trajectory optimizer, it regularizes the geometry of the discrete planner and the differential update law of the execution layer, enabling existing voxel planners to be executed directly on redundant manipulators. From the RL perspective, sequence-modeling approaches that incorporate Q-value regularization—such as Q-Value Regularized Decision ConvFormer (QDC)—highlight the benefits of stabilizing return consistency during trajectory stitching (Ruan et al., 2024). This viewpoint motivates interpreting voxel policies as discrete sequences that require tailored bridging strategies at the geometric and control levels to interface with continuous robot dynamics.

## 3. METHODOLOGY: BRIDGING DISCRETE GEOMETRY AND CONTINUOUS PHYSICS

The method is structured into two tightly coupled layers.

**Geometry Layer.** This layer operates in task space, where a voxel-based Q-learning planner generates a discrete end-effector path using normalized 26-connected actions together with a geometric tie-breaking mechanism.

**Physics Layer.** This layer operates in joint space, where a task-priority damped least-squares (TP-DLS) inverse kinematics solver tracks a smoothed version of the planned path on a 7-DoF manipulator.

In the underlying implementation, the manipulator model internally stores joint configurations in row-vector format when interfacing with standard kinematic routines. For the theoretical development, however, joint configurations are denoted as column vectors  $q \in \mathbb{R}^7$  to maintain consistency with conventional analytical notation. The difference between row and column representations is purely notational and does not affect the underlying kinematic definitions.

Let  $p(q) \in \mathbb{R}^3$  denote the end-effector position obtained from the forward kinematic mapping. The corresponding geometric Jacobian is written as  $J(q) \in \mathbb{R}^{6 \times 7}$ . Its translational component, associated with the positional degrees of freedom, is denoted by  $J_p(q) \in \mathbb{R}^{3 \times 7}$  and corresponds to the upper three rows of  $J(q)$ .

### 3.1 Geometry layer: voxel-based Q-learning and action regularisation

*Q-learning planner on a 3-D voxel grid* The reachable workspace is discretised into a uniform three-dimensional grid of cubic voxels. Let  $\mathcal{S} \subset \mathbb{R}^3$  denote the set of obstacle-free voxel centres. A tabular Q-learning agent is trained on this grid.

At each decision step, the agent occupies a state  $s \in \mathcal{S}$  and selects an action  $a \in \mathcal{A}$ . The environment deterministically maps the pair  $(s, a)$  to a successor state  $s'$  by adding the corresponding voxel offset, and returns a scalar reward  $r$ . The Q-table  $Q(s, a)$  is updated according to

$$Q_{k+1}(s, a) = (1 - \alpha) Q_k(s, a) + \alpha (r + \gamma \max_{a'} Q_k(s', a')) \quad (1)$$

where  $\alpha$  is the learning rate and  $\gamma$  is the discount factor. The reward function follows the reproduced baseline: a positive terminal reward at the goal, a large negative reward for collisions or leaving the grid, and a small step penalty to favour shorter paths and discourage wandering.

After training converges, a greedy policy rolls out a sequence of states

$$s_0, s_1, \dots, s_N, \quad s_k \in \mathcal{S} \quad (2)$$

connecting the start voxel  $s_0$  to the goal voxel  $s_N$ . Mapping each state  $s_k$  to its corresponding Cartesian location yields a discrete end-effector path

$$x_k^{\text{RL}} \in \mathbb{R}^3, \quad k = 0, \dots, N \quad (3)$$

which is the output of the geometry layer before smoothing.

*Normalized 26-Connected Actions with Geometric Tie-Break* The core difference between the proposed planner and the baselines lies in the action geometry and the tie-break rule applied during the policy rollout.

In the proposed planner, the index-space neighbour directions are

$$v = (\Delta i, \Delta j, \Delta k), \quad \Delta i, \Delta j, \Delta k \in \{-1, 0, 1\}, \quad v \neq (0, 0, 0) \quad (4)$$

forming the usual 26-connected neighbourhood. Instead of using these directions directly as grid steps (as in the unnormalized 26-connected baseline), each  $v$  is mapped to a Cartesian displacement with a fixed physical step length  $\delta > 0$ :

$$a(v) = \delta \frac{v}{\|v\|_2} \in \mathbb{R}^3 \quad (5)$$

The resulting action set is

$$\mathcal{A} = \{a_1, \dots, a_{26}\} \quad (6)$$

where each  $a_\ell$  has Euclidean norm  $\|a_\ell\|_2 = \delta$ . This makes the planner isotropic in physical space: axial, face-diagonal, and space-diagonal moves produce the same end-effector displacement magnitude. In the experiments, this eliminates the ‘‘long diagonal step’’ bias of the unnormalized 26-connected planner and provides a more uniform base step length for the execution layer. Crucially, the Q-learning state transitions still occur between discrete voxel centers, but the physical path  $x_k^{\text{RL}}$  is generated using these normalized displacements.

## Bridging Discrete Planning and Continuous Execution for Redundant Robot Manipulators

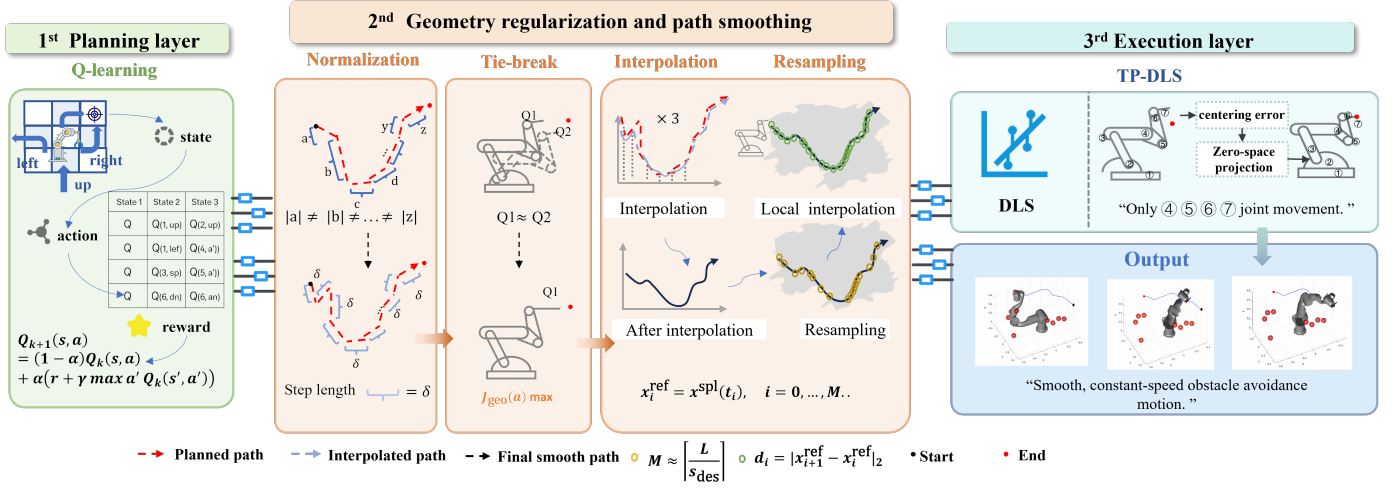


Fig. 2. Overall architecture of the proposed bridging framework combining discrete Q-learning planning, geometric regularization, and continuous TP-DLS execution.

When evaluating the greedy policy after training, it often occurs that several actions at state  $s$  have similar Q-values. If one simply selects arbitrarily among these, the resulting path exhibits unnecessary zig-zag behaviour and frequent changes of direction. To bias the path toward smoother and safer homotopy classes without modifying the Q-update rule, a geometric tie-break is introduced and applied only when there is more than one near-optimal action.

Let

$$Q_{\max}(s) = \max_{a'} Q(s, a') \quad (7)$$

be the largest Q-value at state  $s$ . For a small threshold  $\varepsilon_Q > 0$ , define the set of  $\varepsilon_Q$ -near-optimal actions

$$\mathcal{A}_{\text{tie}}(s) = \{a \in \mathcal{A} : |Q(s, a) - Q_{\max}(s)| < \varepsilon_Q\}. \quad (8)$$

Let  $a_{k-1}$  be the action taken at the previous step, and let  $x$  denote the current end-effector position. For each candidate  $a \in \mathcal{A}_{\text{tie}}(s)$ , compute

$$\begin{aligned} \theta(a, a_{k-1}) & \text{ (turning angle),} \\ d_{\text{obs}}(x, a) & \text{ (approx. look-ahead clearance).} \end{aligned} \quad (9)$$

A geometric score is then defined as

$$J_{\text{geo}}(a) = -w_{\theta} \theta(a, a_{k-1}) + w_d d_{\text{obs}}(x, a) \quad (10)$$

with positive weights  $w_{\theta}$  and  $w_d$ . The selected action is

$$a^* = \begin{cases} \arg \max_{a \in \mathcal{A}_{\text{tie}}(s)} J_{\text{geo}}(a), & \text{if } |\mathcal{A}_{\text{tie}}(s)| > 1, \\ \arg \max_{a \in \mathcal{A}} Q(s, a), & \text{otherwise.} \end{cases} \quad (11)$$

In this way, standard greedy selection  $\arg \max_a Q(s, a)$  is recovered whenever there is a unique  $\varepsilon_Q$ -near-optimal action, while the geometric tie-break only operates when multiple actions have similar Q-values.

For completeness, two baseline planners are also evaluated: *Original*, using a 6-connected action set with grid-resolution step length; and *NoNorm*, using the raw 26-connected index-space directions  $v$  as unnormalized physical steps without a tie-break rule.

*Task-space spline smoothing and micro-step control* The Q-learning planner produces a polyline  $\{x_k^{\text{RL}}\}$  with con-

stant step length  $\delta$ . Although the normalization and tie-breaking mechanisms reduce oscillatory patterns, the path still contains corners. Directly calling inverse kinematics at these points can cause large joint jumps at high-curvature locations.

To obtain a continuous and differentiable reference trajectory for the execution layer, a two-stage smoothing procedure is applied.

First, three independent cubic splines are fitted to the Cartesian coordinates  $(x, y, z)$  of  $\{x_k^{\text{RL}}\}$ , parameterized by the waypoint index  $k$ . This yields a continuous parametric curve:

$$x^{\text{spl}}(t) \in \mathbb{R}^3, \quad t \in [0, 1] \quad (12)$$

Second, the total length  $L$  of the curve is approximated, and a desired macro step size  $s_{\text{macro}}$  (approximately 5 mm in the implementation) is chosen. The number of macro waypoints is then set as

$$M = \left\lfloor \frac{L}{s_{\text{macro}}} \right\rfloor \quad (13)$$

and parameters  $t_i$  are sampled uniformly on  $[0, 1]$  to define

$$x_i^{\text{ref}} = x^{\text{spl}}(t_i), \quad i = 0, \dots, M \quad (14)$$

Consecutive macro waypoints  $\{x_i^{\text{ref}}\}$  are thus approximately arc-length uniform.

Finally, a *micro-step constraint* is enforced within the inverse kinematics routine. If the Euclidean distance between consecutive macro-waypoints exceeds a predefined threshold  $d_{\text{max}}$  (typically  $< 1$  mm), intermediate points are inserted via linear interpolation such that every micro-segment satisfies:

$$\|x_{j+1}^{\text{micro}} - x_j^{\text{micro}}\|_2 \leq d_{\text{max}} \quad (15)$$

This constraint guarantees that the end-effector displacement per TP-DLS iteration remains bounded. This stability is corroborated by the convergence results, where the position error per iteration consistently remains well below the 1 mm threshold.

### 3.2 Physics Layer: Task-Priority Damped Least-Squares Execution

Given the smoothed reference sequence  $\{x_i^{\text{ref}}\}_{i=0}^M$ , the physics layer computes a joint trajectory  $\{q_i\}_{i=0}^M$  on the 7-DoF manipulator. For each reference point  $x_i^{\text{ref}}$ , the solver starts from the previous configuration  $q$  and performs multiple internal iterations of task-priority damped least-squares until the position error falls below a specified tolerance or the maximum iteration count is reached.

*Primary Task: Damped Least-Squares Position Control*  
At a given internal iteration, the position error is

$$e_p = x_i^{\text{ref}} - p(q) \in \mathbb{R}^3 \quad (16)$$

The translational Jacobian is

$$J_p(q) = J_{1:3, \cdot}(q) \in \mathbb{R}^{3 \times 7} \quad (17)$$

and the damped least-squares pseudo-inverse is

$$J_p^\dagger(q) = J_p(q)^\top (J_p(q)J_p(q)^\top + \lambda^2 I_3)^{-1} \quad (18)$$

with scalar damping factor  $\lambda > 0$ . Using a scalar position gain  $k_p > 0$ , the primary joint update is

$$\Delta q_1 = J_p^\dagger(q) k_p e_p \quad (19)$$

The associated null-space projector is

$$N_1(q) = I_7 - J_p^\dagger(q)J_p(q) \quad (20)$$

Orientation tracking is not enforced in the present experiments: the rotational component of the Jacobian is ignored (or equivalently, its gain is set to zero), allowing the end-effector orientation to adapt freely as the solver exploits redundancy.

*Null-space joint-centering objective* To avoid configurations near joint limits and maintain a healthy joint-limit margin, a joint-centering objective is added in the null space of the primary task. Let  $q_{\min}, q_{\max} \in \mathbb{R}^7$  denote the joint limits, and define

$$q_{\text{mid}} = \frac{q_{\min} + q_{\max}}{2} \quad (21)$$

as their midpoint. The joint-centering error is

$$e_c = q_{\text{mid}} - q \quad (22)$$

A simple gradient projection in the null space is applied:

$$\Delta q_2 = \alpha_c N_1(q)^\top e_c \quad (23)$$

with a small gain  $\alpha_c > 0$ . Since  $\Delta q_2$  lies in the null space of the primary task, it does not affect the end-effector position to first order but redistributes the internal posture. This design results in a more balanced minimum joint-limit margin (JointMargin) for TP-DLS compared with the numerical IK baseline.

The unconstrained joint update is therefore

$$\Delta q = \Delta q_1 + \Delta q_2 \quad (24)$$

*Step-Length and Velocity Clipping* Before applying  $\Delta q$  to update the configuration, both a global step-length bound and per-joint bounds are imposed to keep joint displacements and implied velocities within reasonable limits.

Let  $\Delta q_{\max} > 0$  denote the scalar step-length bound. If

$$\|\Delta q\|_2 > \Delta q_{\max} \quad (25)$$

the update is scaled as

$$\Delta q \leftarrow \Delta q \frac{\Delta q_{\max}}{\|\Delta q\|_2} \quad (26)$$

Then, for each joint  $j = 1, \dots, 7$ , an individual bound  $\Delta q_j^{\max} > 0$  is enforced:

$$\Delta q_j \leftarrow \text{clip}(\Delta q_j, -\Delta q_j^{\max}, \Delta q_j^{\max}) \quad (27)$$

where  $\text{clip}(\cdot)$  saturates its argument to the specified interval. Given a nominal time step  $\Delta t$ , these bounds correspond to maximum joint velocities  $|\Delta q_j|/\Delta t \leq \dot{q}_j^{\max}$ .

Finally, the configuration is updated as

$$q \leftarrow q + \Delta q \quad (28)$$

For each reference waypoint  $x_i^{\text{ref}}$ , this procedure is iterated until  $\|e_p\| \leq \varepsilon_p$  with  $\varepsilon_p = 1$  mm, or until a maximum number of internal iterations is reached. If any waypoint fails to meet the tolerance within the iteration limit, the entire trajectory is marked as a failure for that solver. For TP-DLS, the recorded per-iteration errors over all waypoints and tasks form the convergence profile, where virtually all iterations remain within the  $10^{-4} \sim 10^{-3}$  m band, well below the threshold.

As a baseline, a Num-IK executor is also implemented using a conventional numerical inverse kinematics solver. For each reference waypoint, Num-IK solves a full-pose IK problem with the previous solution as initial guess, without task priority, null-space joint centering, or explicit step-length limits. Both executors track the same smoothed reference paths generated by the Improved planner, enabling a fair comparison of joint-space smoothness and safety margins.

The detailed pseudocode of the improved planner and the TP-DLS execution layer is provided in Appendix A.

## 4. EXPERIMENTAL SETUP: FROM SIMULATION TO DATA

This section details the complete experimental workflow conducted on a MATLAB 7-DOF robotic arm simulation platform, ranging from 3D simulation and task set construction to metric evaluation. Instead of focusing on qualitative visual demonstrations, the objective is to establish a systematic and reproducible framework for rigorously assessing the proposed bridging layer.

The controlled system is a 7-DoF robotic manipulator with a typical collaborative robot topology, with joint limits set to the same magnitudes as the physical hardware. This work focuses on the safety distance between the end-effector and obstacles. A collision is considered to occur when the clearance between the end-effector and any obstacle becomes non-positive, i.e., when their inter-center distance is no greater than the sum of their radii. Self-collisions are outside the scope of this paper.

### 4.1 Scenario Classes and Task Set

Static environments are grouped into three density classes according to the number of spherical obstacles:

- **Sparse:** 0–30 obstacles.
- **Medium:** 31–99 obstacles.
- **Dense:** at least 100 obstacles.

Given a density class and a random seed, the scenario generator deterministically samples obstacle positions and radii. For each scenario, a collision-free initial configuration  $q_{\text{start}}$  with sufficient joint margin is selected, its forward kinematics define the start pose, and a target end-effector pose  $x_{\text{goal}}$  is specified. Candidate  $q_{\text{goal}}$  configurations are obtained by inverse kinematics; solutions in collision or too close to joint limits are discarded and one feasible  $q_{\text{goal}}$  is kept.

For every density class, 1,000 start-goal pairs are generated, giving 3,000 tasks in total. All statistics are computed over this task set and reported per density class.

#### 4.2 Planner Configurations

At the planning layer, a Q-learning voxel-grid planner is used as a black box. The state space, reward design, and learning hyperparameters are identical in all comparisons; only the action geometry differs:

- **Original:** 6-neighbour actions, allowing motion along the three coordinate axes with step size equal to the grid resolution.
- **NoNorm:** unnormalized 26-neighbour actions, allowing transitions to all adjacent voxels with different Euclidean step lengths for axial and diagonal moves.
- **Improved (proposed):** 26-neighbour actions normalized to a uniform physical step length, combined with a geometric tie-breaking rule based on turning angle and local clearance when Q-values are nearly equal.

All planners share the same learning rate, discount factor, and  $\varepsilon$ -greedy exploration. After convergence, each planner produces a discrete end-effector path for every task. The resulting voxel sequences are mapped to Cartesian space, fitted with a cubic spline, and resampled at approximately equal arc length to obtain a smooth reference path. This path is used both to evaluate planner geometry (length, turns, clearance) and as the common input to the execution layer.

#### 4.3 Execution Layer Configurations

To isolate the execution-layer effect, all executors operate on the same smooth reference paths generated by the Improved planner; only the inverse kinematics strategy is changed.

**Num-IK.** A toolbox-based numerical IK baseline. For each reference waypoint, `inverseKinematics` is called independently, using the previous solution as the initial guess. Redundancy is not exploited and joint increments are not explicitly bounded.

**TP-DLS (proposed).** A task-priority damped least-squares scheme, with end-effector position tracking as the primary task and joint centering as a soft null-space objective. Both the norm of the joint increment and each joint component are clamped at every step, effectively regulating joint velocities and accelerations.

In this way, differences in execution quality can be attributed to the IK strategy rather than to differences in the planned path.

#### 4.4 Data Pipeline and Metrics

For each task, planner outputs and joint trajectories are recorded and processed by a unified script that computes all metrics.

Planner-level metrics are: success rate, path length, number of turns, number of discrete steps, and minimum end-effector-obstacle distance. Execution-level metrics are: the 95th percentile of the joint increment norm, maximum joint velocity, maximum joint acceleration, minimum joint-limit margin, number of backtracks or retries, and total computation time.

For planner comparison, tasks that fail to reach the goal are assigned fixed penalty values for length, turns, and step count, so that feasibility and path quality can be evaluated jointly. For execution-layer comparison, the planner is fixed to the improved variant.

## 5. RESULTS AND DISCUSSION

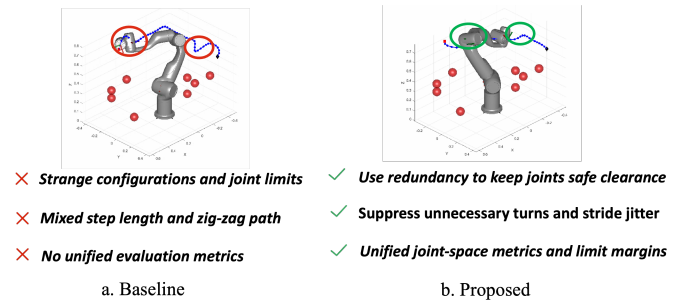


Fig. 3. **Qualitative comparison on a 7-DoF arm.** (a) Baseline (unnormalised actions + Num-IK) shows irregular steps and joint-limit configurations. (b) Proposed bridge (normalised 26-neighbour + TP-DLS) equalises step size and keeps joints away from limits.

#### 5.1 Planning Interface Regularization

Table 1 reports the planning metrics for the three planners over 150 queries. The *Original* and *NoNorm* baselines reach only 0.56–0.70 success rate, with most failures occurring in dense scenes. The proposed *Improved* planner achieves 1.00 success rate under all obstacle densities.

Regarding geometric quality, the *Improved* method consistently produces shorter paths with fewer turns than both baselines, especially in dense environments. Minimum-clearance values, however, remain nearly identical across all methods, indicating that the improvements do not trade clearance for path length. Instead, step normalization and geometric tie-breaking reduce the irregular step alternation and backtracking inherent in the unnormalized 26-neighbor expansion. Step-size statistics further show that the *Improved* planner yields highly uniform waypoint spacing, which is beneficial for subsequent spline interpolation and DLS tracking.

#### 5.2 Impact of Execution Layer on Trajectory Quality

For the execution layer comparison, the planner is fixed to *Improved* for all 150 tasks. Since both solvers track

Table 1. Three Planners Under Different Obstacle Densities

Density	Algorithm	Success rate	Length	Turns	MinClearance	Steps
Sparse	Original	0.68	192.572	1862.9	0.213	2126.72
Sparse	NoNorm	0.6	283.35	1451.42	0.213	2563.84
Sparse	Improved	<b>1.0</b>	<b>0.602</b>	<b>4.26</b>	0.216	<b>7.02</b>
Medium	Original	0.68	168.516	1681.98	0.157	1926.16
Medium	NoNorm	0.7	195.7	1122.5	0.152	1725.12
Medium	Improved	<b>1.0</b>	<b>0.598</b>	<b>3.98</b>	0.165	<b>6.98</b>
Dense	Original	0.56	396.468	3901.6	0.125	3965.68
Dense	NoNorm	0.58	499.377	3237.8	0.119	3783.9
Dense	Improved	<b>1.0</b>	<b>0.68</b>	<b>5.02</b>	0.138	<b>7.8</b>

Table 2. Two Execution Layers Under the Same Reference Trajectory

Density	Solver	Success_rate	DQ_95	MaxVel	MaxAcc	JointMargin	Backtracks	Time
Sparse	Num-IK	1.0	0.8211	141.8634	12701.6607	0.0053	7.18	0.7231
Sparse	TP-DLS	1.0	<b>0.0113</b>	<b>84.2102</b>	<b>3943.5816</b>	<b>0.0126</b>	19.44	35.9558
Medium	Num-IK	1.0	0.6415	190.3101	16793.8613	0.0045	6.5	0.6859
Medium	TP-DLS	1.0	<b>0.0113</b>	<b>79.747</b>	<b>3860.0759</b>	<b>0.0112</b>	37.6	36.7482
Dense	Num-IK	1.0	0.937	175.8501	15659.236	0.0002	5.48	0.6497
Dense	TP-DLS	1.0	<b>0.0088</b>	<b>91.651</b>	<b>4438.005</b>	<b>0.014</b>	22.16	29.0056

identical task-space trajectories, metrics such as path length, number of turns, and minimum clearance remain virtually unchanged, and both maintain position errors within 1 mm for all reference points, achieving a success rate of approximately 100%.

Table 2 reveals that TP-DLS exhibits an order-of-magnitude advantage over the numerical IK baseline in terms of  $DQ_{95}$ . Across all obstacle densities, TP-DLS keeps  $DQ_{95}$  on the order of  $10^{-2}$  rad, whereas *NumIK* ranges from  $10^{-1}$  to  $10^0$  rad. In representative trajectories, maximum joint increments remain below the 0.1-rad warning threshold, causing the curve to remain nearly flat. Likewise, TP-DLS substantially reduces *MaxVel* and *MaxAcc*, suppressing the abrupt joint transitions and dynamic spikes typical of numerical IK.

Statistics for *JointMargin* show that both solvers maintain comparable margins from joint limits. TP-DLS holds a slight advantage in most tasks, suggesting that the subordinate joint-centering task in the null space does not compromise safety but rather increases the distance from limits in certain scenarios. Conversely, TP-DLS achieves these improvements at a higher computational cost: both *Backtracks* and *Time* are notably higher than those of *NumIK*, reflecting the strategy of employing multiple small-step iterations and retries in locally challenging sections. Given that this work focuses on offline evaluation, this computational overhead remains within an acceptable range. Both solvers maintain similar *JointMargin* values, with TP-DLS showing a mild advantage, indicating that its null-space joint-centering does not compromise safety.

In representative dense scenarios, the final position error of interpolated reference points for TP-DLS stabilizes within the range of  $10^{-4}$  to  $10^{-3}$  m, consistently remaining below the 1 mm threshold. The vast majority of error points during iterations cluster within a narrow band near  $10^{-4}$  m, with only a few initial points corresponding to the phase of approaching the trajectory neighborhood from the initial configuration, showing no widespread numerical divergence. This demonstrates the stable convergence and reliable trajectory tracking performance of TP-DLS across multiple tasks and scenarios.

## 6. CONCLUSION

This work addresses the common robotic RL planning paradigm characterized by “voxel grids + finite neighborhood actions + Q-learning.” Without modifying the underlying planning algorithm, we propose a bridging framework between discrete planning and continuous execution for 7-DoF redundant manipulators. On the planning side, the introduction of step-normalized 26-neighbor actions and a geometric tie-breaking mechanism explicitly eliminates the geometric anisotropy of discrete actions. This significantly reduces path length and the number of turns while improving success rates in complex obstacle scenarios, all without compromising minimum clearance. On the execution side, a TP-DLS inverse kinematics layer, combined with task-space spline smoothing and step-limited interpolation, achieves millimeter-level end-effector accuracy and substantially improved joint smoothness. Consequently, the 95th-percentile joint increments and dynamic peaks are compressed to levels far lower than those of traditional numerical IK.

Since this bridging layer relies solely on the discrete end-effector path output by the planner and remains agnostic to the specific RL algorithm or network structure, it serves as a generic interface that effectively decouples existing grid-based RL planning from the continuous control of redundant manipulators. Future work will integrate this method with safety filtering techniques to achieve online execution with formal safety guarantees. Additionally, we aim to validate its applicability and limitations on physical robot platforms and in more complex tasks, such as multi-arm coordination and dexterous manipulation.

## REFERENCES

- Basso, E.A. and Pettersen, K.Y. (2020). Task-priority control of redundant robotic systems using control lyapunov and control barrier function based quadratic programs. *IFAC-PapersOnLine*, 53(2), 9037–9044.
- Deo, A.S. and Walker, I.D. (1995). Overview of damped least-squares methods for inverse kinematics of robot manipulators. *Journal of Intelligent and Robotic Systems*, 14(1), 43–68.

Elguea-Aguinaco, Í., Inziarte-Hidalgo, I., Bøgh, S., and Arana-Arexolaleiba, N. (2024). A review on reinforcement learning for motion planning of robotic manipulators. *International Journal of Intelligent Systems*, 2024(1), 1636497.

Han, D., Mulyana, B., Stankovic, V., and Cheng, S. (2023). A survey on deep reinforcement learning algorithms for robotic manipulation. *Sensors*, 23(7), 3762.

James, S., Wada, K., Laidlow, T., and Davison, A.J. (2022). Coarse-to-fine q-attention: Efficient learning for visual robotic manipulation via discretisation. In *Proceedings of the IEEE/CVF Conference on Computer Vision and Pattern Recognition*, 13739–13748.

Jia, Y., Li, Y., Xin, B., and Chen, C. (2020). Path planning with autonomous obstacle avoidance using reinforcement learning for six-axis arms. In *2020 IEEE International Conference on Networking, Sensing and Control (ICNSC)*, 1–6. IEEE.

Kim, J., Jin, M., Park, S.H., Chung, S.Y., and Hwang, M.J. (2020). Task space trajectory planning for robot manipulators to follow 3-d curved contours. *Electronics*, 9(9), 1424.

Landgraf, C., Meese, B., Pabst, M., Martius, G., and Huber, M.F. (2021). A reinforcement learning approach to view planning for automated inspection tasks. *Sensors*, 21(6), 2030.

Li, X., Liu, H., and Dong, M. (2021). A general framework of motion planning for redundant robot manipulator based on deep reinforcement learning. *IEEE Transactions on Industrial Informatics*, 18(8), 5253–5263.

Liu, Y., Zha, F., Li, M., Guo, W., Jia, Y., Wang, P., Zang, Y., and Sun, L. (2021). Creating better collision-free trajectory for robot motion planning by linearly constrained quadratic programming. *frontiers in Neurobotics*, 15, 724116.

Nakamura, Y., Hanafusa, H., and Yoshikawa, T. (1987). Task-priority based redundancy control of robot manipulators. *The International Journal of Robotics Research*, 6(2), 3–15.

Pan, J., Zhang, L., and Manocha, D. (2012). Collision-free and smooth trajectory computation in cluttered environments. *The International Journal of Robotics Research*, 31(10), 1155–1175.

Ruan, Z., Yan, T., Cai, Y., Han, Y., Zheng, L., and Zhang, Y. (2024). Q-value regularized decision convformer for offline reinforcement learning. In *2024 IEEE International Conference on Robotics and Biomimetics (RO-BIO)*, 91–97. IEEE.

Zhong, B., Lavaei, A., Cao, H., Zamani, M., and Caccamo, M. (2021). Safe-visor architecture for sandboxing (ai-based) unverified controllers in stochastic cyber-physical systems. *Nonlinear Analysis: Hybrid Systems*, 43, 101110.

Zhong, B., Liu, S., Caccamo, M., and Zamani, M. (2023). Secure-by-construction controller synthesis via control barrier functions. *IFAC-PapersOnLine*, 56(2), 239–245.

## Appendix A. PSEUDOCODE OF THE PLANNING-EXECUTION BRIDGE

---

**Algorithm 1** Improved RL planner and reference path

---

**Require:** start/goal  $x_s, x_g \in \mathbb{R}^3$ ; obstacles  $\mathcal{O}$ ; Q-table  $Q$ ; step  $\delta$ ; macro step  $s_{\text{mac}}$ ; micro step  $d_{\text{max}}$

**Ensure:** reference waypoints  $X_{\text{ref}} = \{x_i\}$

- 1:  $s \leftarrow \text{VOXELFROMPOS}(x_s)$
- 2:  $s_G \leftarrow \text{VOXELFROMPOS}(x_g)$
- 3:  $k \leftarrow 0$ ;  $X_{\text{RL}} \leftarrow [\text{POSFROMVOXEL}(s)]$ ;  $a_{\text{prev}} \leftarrow \text{NULL}$
- 4: **while**  $s \neq s_G$  **and**  $k < K_{\text{max}}$  **do** ▷ RL rollout on normalized 26-neighbourhood
- 5:    $Q_{\text{max}} \leftarrow \max_a Q(s, a)$
- 6:    $\mathcal{A}_{\text{tie}} \leftarrow \{a \in \mathcal{A} \mid |Q(s, a) - Q_{\text{max}}| < \varepsilon_Q\}$
- 7:   **if**  $|\mathcal{A}_{\text{tie}}| > 1$  **then** ▷ true tie: several near-optimal actions
- 8:      $a^* \leftarrow \arg \max_{a \in \mathcal{A}_{\text{tie}}} J_{\text{geo}}(a, a_{\text{prev}}, X_{\text{RL}}[k], \mathcal{O})$
- 9:     **else** ▷ unique winner: fall back to greedy
- 10:      $a^* \leftarrow \arg \max_{a \in \mathcal{A}} Q(s, a)$
- 11:    $s \leftarrow \text{NEXTSTATE}(s, a^*, \delta)$
- 12:    $a_{\text{prev}} \leftarrow a^*$
- 13:   append  $\text{POSFROMVOXEL}(s)$  to  $X_{\text{RL}}$
- 14:   **if**  $\text{COLLISION}(X_{\text{RL}}[k+1], \mathcal{O})$  **then**
- 15:     **break**
- 16:    $k \leftarrow k + 1$
- 17:  $X^{\text{mac}} \leftarrow \text{SPLINERESAMPLE}(X_{\text{RL}}, s_{\text{mac}})$
- 18:  $X_{\text{ref}} \leftarrow \text{SUBDIVIDE}(X^{\text{mac}}, d_{\text{max}})$

---

**Algorithm 2** TP-DLS execution along the reference path

---

**Require:**  $X_{\text{ref}} = \{x_i^{\text{ref}}\}$ ; robot model; end-effector name;  $q_0$ ; joint limits  $q_{\text{min}}, q_{\text{max}}$ ; damping  $\lambda$ ; gain  $k_p$ ; null-space gain  $\alpha_c$ ; bounds  $\Delta q_{\text{max}}, \{\Delta q_{\text{max}, j}\}$ ; tolerance  $\varepsilon_p$ ; max iterations  $K_{\text{max}}$

**Ensure:** joint trajectory  $Q = \{q[i]\}$ ; success flag

- 1:  $q \leftarrow q_0$ ;  $q_{\text{mid}} \leftarrow \frac{1}{2}(q_{\text{min}} + q_{\text{max}})$ ;  $Q[0] \leftarrow q$
- 2: **for**  $i = 0$  **to**  $|X_{\text{ref}}| - 1$  **do**
- 3:    $x^* \leftarrow x_i^{\text{ref}}$ ;  $k \leftarrow 0$
- 4:   **repeat**
- 5:      $x \leftarrow \text{FORWARDPOS}(\text{robot}, q)$
- 6:      $e_p \leftarrow x^* - x$
- 7:     **if**  $\|e_p\| \leq \varepsilon_p$  **then**
- 8:       **break**
- 9:      $J \leftarrow \text{GEOMJACOBIAN}(\text{robot}, q)$
- 10:      $J_p \leftarrow J_{1:3,:}$  ▷ translational block
- 11:      $J_p^\dagger \leftarrow J_p^\top (J_p J_p^\top + \lambda^2 I_3)^{-1}$
- 12:      $\Delta q_1 \leftarrow J_p^\dagger (k_p e_p)$
- 13:      $N_1 \leftarrow I_7 - J_p^\dagger J_p$
- 14:      $e_c \leftarrow q_{\text{mid}} - q$
- 15:      $\Delta q_2 \leftarrow \alpha_c N_1^\top e_c$
- 16:      $\Delta q \leftarrow \Delta q_1 + \Delta q_2$
- 17:      $\Delta q \leftarrow \text{CLIPNORM}(\Delta q, \Delta q_{\text{max}})$
- 18:     **for**  $j = 1$  **to**  $7$  **do**
- 19:        $\Delta q_j \leftarrow \text{CLIP}(\Delta q_j, -\Delta q_{\text{max}, j}, \Delta q_{\text{max}, j})$
- 20:      $q \leftarrow q + \Delta q$ ;  $k \leftarrow k + 1$
- 21:     **until**  $k \geq K_{\text{max}}$
- 22:     **if**  $\|e_p\| > \varepsilon_p$  **then**
- 23:       **return**  $(Q, \text{FALSE})$
- 24:    $Q[i+1] \leftarrow q$
- 25: **return**  $(Q, \text{TRUE})$

---